

Validating Time-Distance Far-side Imaging of Solar Active Regions through Numerical Simulations

Thomas Hartlep¹, Junwei Zhao², Nagi N. Mansour¹, and Alexander G. Kosovichev²

ABSTRACT

Far-side images of solar active regions have become one of the routine products of helioseismic observations, and are of importance for space weather forecasting by allowing the detection of sunspot regions before they become visible on the Earth side of the Sun. An accurate assessment of the quality of the far-side maps is difficult, because there are no direct observations of the solar far side to verify the detections. In this paper we assess far-side imaging based on the time-distance helioseismology method, by using numerical simulations of solar oscillations in a spherical solar model. Localized variations in the speed of sound in the surface and subsurface layers are used to model the perturbations associated with sunspots and active regions. We examine how the accuracy of the resulting far-side maps of acoustic travel times depends on the size and location of active regions. We investigate potential artifacts in the far-side imaging procedure, such as those caused by the presence of active regions on the solar near side, and suggest how these artifacts can be identified in the real Sun far-side images obtained from SOHO/MDI and GONG data.

Subject headings: methods: numerical — Sun: helioseismology — Sun: oscillations — sunspots

1. INTRODUCTION

Imaging of active regions on the far side of the Sun, the side facing away from Earth, is a valuable tool for space weather forecasting, as well as for studying the evolution of active regions. It allows monitoring of active regions before they rotate into the near side, and after they rotate back into the far side. Far-side images are produced daily by the acoustic holography technique (Lindsey & Braun 2000a) using observations from both the Global Network

¹NASA Ames Research Center, M/S 230-2, Moffett Field, CA 94035-1000

²W. W. Hansen Experimental Physics Laboratory, Stanford University, Stanford, CA 94305-4085

Oscillation Group (GONG), and the Michelson Doppler Imager (MDI) on board the Solar and Heliospheric Observatory (SOHO). Lindsey & Braun (2000a) and Duvall & Kosovichev (2001) have pioneered the solar far-side imaging work, mapping the central region of the far-side Sun by analyzing acoustic signals for double-skip ray paths on both sides of the far-side region, by use of helioseismic holography (for a review, see Lindsey & Braun 2000b) and time-distance helioseismology (Duvall et al. 1993) techniques, respectively. Braun & Lindsey (2001) further developed their technique to map the near-limb and polar areas of the solar far side by combining single- and triple-skip acoustic signals. More recently, Zhao (2007) has developed a five-skip time-distance imaging scheme that measures travel times of a combination of double- and triple-skip acoustic wave signals. Combined with the traditionally used four-skip far-side imaging schemes, the new technique greatly reduces the noise level in far-side images, as well as helps to remove some of the spurious features visible in the four-skip images.

In general terms, far-side imaging by time-distance helioseismology detects changes in the travel time for acoustic waves traveling through an active region compared to those traveling only in the quiet Sun, while helioseismic holography detects phase shifts in acoustic wave signals. The exact mechanisms of how the presence of an active region causes the observed variations are not fully understood, although, it is generally believed that a change of the magnetoacoustic wave speed inside active regions (Kosovichev & Duvall 1997; Kosovichev et al. 2000; Zhao & Kosovichev 2006) plays an important role. Also, it has been argued that strong surface magnetic fields associated with active regions (Fan et al. 1995; Lindsey & Braun 2005) may affect inferences obtained by the acoustic holography technique; however, Zhao & Kosovichev (2006) have shown that these effects are not a major factor in the determination of the interior structure of sunspots by time-distance helioseismology.

Far-side imaging has been successful for predicting the appearance of large active regions and complexes of activity. However, it is unclear how robust and accurate the far-side imaging techniques are, and how much we should believe in the far-side images that are being produced daily. Past efforts have tried to evaluate the accuracy of far-side images by comparing them with the directly observed Earth-side images just after active regions have rotated into view from the far side, or before they have rotated out of view into the far side (González Hernández et al. 2007). However, active regions may develop quite fast, emerging or disappearing on a time scale of days or even less. Therefore, such analyses are not sufficient. On the other hand, numerical modeling of solar oscillations can provide artificial data that can enable evaluating and improving these methods. In a global solar model, we can place near-surface perturbations mimicking active regions on the far side of the modeled Sun, and apply helioseismic imaging techniques to the simulated wavefield. The resulting far-side images can be compared directly with the precisely known properties of

the perturbations, allowing for a more accurate evaluation of the capabilities and limitations of the far-side imaging techniques.

In this paper, we present results on testing the recently improved time-distance helioseismology far-side imaging technique (Zhao 2007) by using 3D numerical simulations of the oscillations in the global Sun. We assess the sensitivity of the imaging technique by varying the size and location of a sound speed perturbation mimicking a single active region. In other simulations, we place two active regions at the solar surface in order to examine whether the acoustic waves traveling through the active regions may interfere with each other and affect the imaging of the other region. Finally, we identify one scenario in which artifacts (“ghost images”) caused by an active region on the near side appear in the far-side maps. A brief description of the simulation technique is given in § 2, followed by a description of the far-side imaging procedure in § 3. The main results are presented in § 4, and a discussion and concluding remarks are given in § 5.

2. NUMERICAL SIMULATION

2.1. Simulation Code

In the following, we briefly describe the numerical simulation code used in this study. For more details, the reader is referred to Hartlep & Mansour (2005), and in particular, to a detailed description of the code, which will be published soon (Hartlep & Mansour, in preparation).

Simulating the 3D wavefield in the full solar interior is not an easy task, and many simplifications have to be made to make such simulations feasible on currently available supercomputer systems. For the present case, we model solar acoustic oscillations in a spherical domain by using linearized Euler equations and consider a static background in which only localized variations of the sound speed are taken into account. The oscillations are assumed to be adiabatic, and are driven by randomly forcing density perturbations near the surface. For the unperturbed background model of the Sun, we use the standard solar model S of Christensen-Dalsgaard et al. (1996) matched to a model for the chromosphere (Vernazza et al. 1981). Localized sound speed perturbations of various sizes are added in the surface and subsurface layers to mimic the perturbations of the wave speed associated with sunspots and active regions. Non-reflecting boundary conditions are applied at the upper boundary by means of an absorbing buffer layer with a damping coefficient that is zero in the interior and increases smoothly into the buffer layer.

The linearized Euler equations describing wave propagation in the Sun are written in

the form:

$$\partial_t \rho' = -\Phi' + S - \chi \rho', \quad (1)$$

$$\partial_t \Phi' = -\Delta c_0^2 \rho' + \nabla \cdot \rho' \mathbf{g}_0 - \chi \Phi', \quad (2)$$

where ρ' and Φ' are the density perturbations and the divergence of the momentum perturbations associated with the waves, respectively. S is a random function mimicking acoustic sources, c_0 is the background sound speed, \mathbf{g}_0 is the acceleration due to gravity, and χ is the damping coefficient of the absorbing buffer layer. Perturbations of the gravitational potential have been neglected, and the adiabatic approximation has been used. In order to make the linearized equations convectively stable, we have neglected the entropy gradient of the background model. The calculations show that this assumption does not significantly change the propagation properties of acoustic waves including their frequencies, except for the acoustic cut-off frequency, which is slightly reduced. This is quite acceptable for our purpose, because the part of the spectrum that is actually used in the far-side imaging technique lies well below this cut-off frequency. For comparison, other authors have modified the solar model including its sound speed profile (e.g. Hanasoge et al. 2006; Parchevsky & Kosovichev 2007). In those cases, the oscillation mode frequencies may differ significantly from the real Sun frequencies.

Starting from Eqs. (1) and (2), we absorb the damping terms $\chi \rho'$ and $\chi \Phi'$ into the other terms by use of an integrating factor, and apply a Galerkin scheme for the numerical discretization. Spherical harmonic functions are used for the angular dependencies, and 4th order B-splines (Loulou et al. 1997; Kravchenko et al. 1999) for the radial direction. 2/3-dealiasing is used in the computations of the $c_0^2 \rho'$ -term in angular space, while all other operations are performed in spherical harmonic coefficient space. The radial resolution of the B-spline method is varied proportionally to the local speed of sound, i.e. the generating knot points are closely spaced near the surface (where the sound speed is small), and are coarsely spaced in the deep interior (where the sound speed is large). The simulations presented in this paper employ the spherical harmonics of angular degree l from 0 to 170, and 300 B-splines in the radial direction. A staggered Yee scheme (Yee 1966) is used for time integration, with a time step of 2 seconds.

The oscillation power spectrum as a function of spherical harmonic degree l computed for one of the performed simulations is shown in Figure 1. It is found that the frequencies of the ridges correspond well with the frequencies from solar observations. As noted before, the model has a lower cut-off frequency, but this does not pose a problem for our purposes. Also, Figure 1 shows a time-distance diagram (i.e., the mean cross-covariance function) calculated for the same simulation data. Even though no filtering has been done for computing the time-distance correlations, both the four-skip and five-skip acoustic signals needed for the

far-side imaging technique are clearly visible. In fact, these correlations are stronger than in observational data, where it is essential to filter out other unwanted wave components (compare, e.g. Zhao 2007). The acoustic travel times are fairly close to those found in solar observations. Even for the long travel times of four- and five-skip signals, the discrepancy between the simulations and the observations is only about 1.2 minutes, or 0.2 percent.

2.2. Active Region Model

Solar active regions are complex structures and are believed to differ from the quiet Sun in their temperature, density, and sound speed distributions, and include complicated flow and magnetic field configurations. The acoustic wave speed variations inside active regions due to temperature changes and magnetic fields has, for obvious reasons, a very direct effect on the travel times. For this investigation, we model active regions by local sound speed perturbations, which include the combined temperature and magnetic effects (Kosovichev et al. 2000), but leave it to a later investigation to include plasma flows. Since the main goal of the current far-side imaging efforts is to detect the locations of active regions and estimate their size, this is quite sufficient. We model a solar active region by a circular region in which the sound speed c differs from the quiet Sun sound speed c_o in the following fashion:

$$(c/c_o)^2 = 1 + f(\alpha)g(h), \quad (3)$$

where α is the angular distance from the center of the active region, h the radial distance from the photosphere, and

$$f(\alpha) = \begin{cases} 1 + \cos(\pi\alpha/\alpha_d) & \text{for } |\alpha| \leq \alpha_d; \\ 0 & \text{otherwise.} \end{cases} \quad (4)$$

The radial profile $g(h)$ of the prescribed sound speed perturbation is shown in Figure 2. The profile has been derived by inversions of the time-distance measurements of an actual sunspot (Kosovichev et al. 2000), and confirmed by a number of other local helioseismology inversions (Jensen et al. 2001; Sun et al. 2002; Basu et al. 2004; Couvidat et al. 2006; Zharkov et al. 2007). Some of these studies have shown that the significant sound speed perturbation associated with the sunspot structure probably extends deeper than what was originally inferred. Also, investigations of large active regions by Kosovichev & Duvall (2006) have indicated that the perturbations are extended significantly deeper than those for the relatively small and isolated sunspot in Kosovichev et al. (2000). Therefore, we extended this profile into the deeper layers as shown in Figure 2. The simulations have been performed for three different active region horizontal sizes α_d corresponding to radii at the solar surface of

45, 90 and 180 Mm, respectively. Effects of structure variations with depth or the strength of the perturbations have not been studied.

3. FAR-SIDE IMAGING PROCEDURE

Zhao (2007) has imaged the solar far side using medium- l data acquired by SOHO/MDI (Scherrer et al. 1995). MDI medium- l data consist of line-of-sight photospheric velocity images with a cadence of 1 minute and a spatial sampling of 0.6° per pixel (here and after, degree means heliographic degree). The data are mapped into heliographic coordinates using Postel’s projection, and only the central $120^\circ \times 120^\circ$ region of the solar disk is used for the far-side imaging analysis. The observational time series were 2048 minutes long.

From the simulations, very similar datasets were generated. Radial velocity maps were computed at a location of 300 km above the photosphere, approximately at the formation height of MDI Dopplergrams (Norton et al. 2006), and stored with a 1-minute cadence and a spatial resolution of 0.703° per pixel, slightly lower than the resolution of the MDI data. The region selected for the analysis was of the same size, $120^\circ \times 120^\circ$, as in the analysis of the MDI observations. The first 500 minutes of each simulation were discarded as they represent transient behavior, and the following 1024 minutes were used in the analysis. This is only half of the duration used in the observational analysis, but as Figure 1 shows, four- and five-skip acoustic signals are sufficiently strong to perform the far-side analysis even with such a relatively short period.

The rest of the procedure for the simulation data is the same as for the observations presented in Zhao (2007). After the remapping, the data are filtered in the Fourier domain, and only waves that travel long enough to return to the near side from the back side after four and five rebounces are kept. The time-distance cross-covariance function is computed for points inside the annuli as indicated in Figure 3. The locations and sizes of these annuli depend on the measurement scheme. For the four-skip scheme and the double-double skip combination, the annulus covers a range of distances of $133.8^\circ - 170.0^\circ$ from the targeted point on the far side. For the single-triple combination, this range is $66.9^\circ - 85.0^\circ$ for the single skip, and $200.7^\circ - 255.0^\circ$ for triple skip. For the five-skip scheme, the annulus covers the range of $111.6^\circ - 174.0^\circ$ from the targeted point for the double skip, and $167.4^\circ - 261.0^\circ$ for the triple skip. The four-skip scheme can recover images of 190° in longitude (5° past the limb to the solar near side on either limb), while the five-skip scheme recovers a total of 160° in longitude, somewhat less than the whole far side. As usual, the cross-covariance functions for different distances are combined after appropriate shifts in time based on ray theory predictions. The final cross-covariance functions are fitted using a Gabor wavelet

(Kosovichev & Duvall 1997) to derive the acoustic phase travel times for the four- and five-skip schemes separately. After a mean background travel time is subtracted from each map, the residual travel times maps show variations, corresponding to active regions on the far side.

4. RESULTS

4.1. Sensitivity

In order to examine the sensitivity of the time-distance far-side imaging technique to the size of active regions, we have simulated the global acoustic wave fields for solar models with sound speed perturbations of 3 different values of their radius: 180 Mm (large), 90 Mm (medium), and 45 Mm (small). The radial structure of the sound speed perturbation has been given in Sec. 2.

Figure 4 presents the case when a medium-sized active region is located at the far-side center (directly opposite to the observer). It can be seen that both four- and five-skip measurement schemes can recover this far-side region, but with some level of spurious features. The combined image from both schemes gives a better active region image, though not completely clear of spurious features. The images are displayed with thresholds of -3.5σ to -2σ , where σ is the standard deviation of the travel-time perturbations, in order to isolate the strong negative signals associated with active regions. The original unrestricted image without thresholding, and the corresponding probability distribution function of the travel time residuals are shown in Figure 5. In this particular case, σ is of the order of 12 seconds for the combined image. For comparison, a lower value of 3.3 seconds was found in observations (Zhao 2007). The noise level depends on the stochastic properties of solar waves and the length of the data time series. This probably explains the difference in the noise levels. However, this difference is not significant for this study since we measure the signal relative to the noise level.

Figure 6 shows the same, medium-sized active region, but now located closer to the far-side limb. Once again, the combined far-side image gives the best result. It is clear from both Figures 4 and 6 that the time-distance technique determines the size and location of the far-side active regions well but fails to accurately image their shape.

Figure 7 presents the travel-time images combined from the four- and five-skip measurements for the simulations of the large active region. It is evident that the time-distance technique gives the correct size, location, and even shape of the far-side active regions for both far-side locations: at the center, and near the limb.

For the case with a small active region (45 Mm radius), the time-distance helioseismology imaging fails to provide any credible signature of the existence of the region on the far side. The travel-time maps are not shown for this case, since they don’t show any significant features. Of course, it should come as no surprise that the imaging technique has a lower limit on what size of active region can be detected. The time-distance far-side imaging method used in this study employs only the oscillation modes with spherical harmonic degrees l between 3 and 50. It is conceivable that structures comparable in size or even smaller than the horizontal wavelength of the acoustic waves used in the analysis will have little effect on such waves. Such small structures would be hard or impossible to detect. A simple estimate of the node-to-node distance for a spherical harmonic of degree 50 (the highest used in the analysis) gives about 90 Mm at the surface, or twice the radius of the small active region.

It is quite common that multiple active regions are present on the Sun. Some of them may produce perturbations of the wave field, which may interfere with the perturbation of a targeted active region. In order to examine whether the different regions would interfere with each other in the far-side images, we performed a simulation with two medium-sized active regions located at the solar equator, 150° apart from each other. We have examined various different far-side locations of the active regions, and two examples are presented in Figure 8. In all cases we found that these two active regions do not interfere with each other. Both active regions have been imaged correctly as if they were the sole regions on the Sun, except that some “ghost images” appeared under certain circumstances. However, such artifacts also appear for a single active region case under the same circumstances, as described in the next section.

For convenience, the active regions in the numerical experiments were placed on the far-side equator. On the real Sun, though, active regions are often far from the equator, and one may be confronted with additional effects such as foreshortening and line-of-sight projection. However, these effects are expected to be small because only oscillations of relatively low angular degrees are used in the analysis and also because of the rather small observing window extending only 60° from the disk center. To test this expectation, we have performed an additional numerical experiment with a medium-sized active region placed at a latitude of 20° above the equator, used line-of-sight velocities instead of the pure radial velocities, and included the effect of foreshortening. The results were not significantly different from those in Figure 4.

4.2. Ghost Images

It is found that when an active region is placed at certain locations, a “ghost image” of the active region may appear in the far-side image. Figure 9 presents two such examples when an active region on the near side is close to the limb. A “ghost image” appears approximately at the antipode of this active region, with a weaker acoustic travel time signal and smaller in size. Note that because of the selection of very small l ’s when computing far-side images, the spatial resolution of images is only about 10° . Therefore, the “ghost image” may appear several degrees away from the antipode of the region.

Given the measurement scheme, it is very reasonable to expect such an artifact when the active region is located close to the near-side limb. Consider, for example, a single-triple skip combination in the four-skip measurement scheme. If we select an annulus 70° from a targeted far-side quiet region, this annulus is also 250° away from that quiet region’s antipode. If an active region is located there, acoustic waves with travel time deficits caused by that active region are not filtered out because their distance range also falls in the triple-skip range in our analysis (compare annulus radii in Sec. 3).

5. DISCUSSION

We have successfully simulated the global acoustic wavefield of the Sun and have used the simulation data to validate the time-distance far-side imaging technique for two measurement schemes with four and five skips of the acoustic ray paths.

We have found that this technique is able to reliably detect our model active regions with radii of 90 Mm and 180 Mm. The locations and sizes of the far-side active regions are determined correctly, although, their shapes are often slightly different from the original. Expectedly, larger active regions are easier to detect, and their images are more clear. For the small active region of 45 Mm radius, the far-side imaging method fails since it is below the resolution limit. In the case of more than one active regions present on the solar surface, we have found that they do not affect each other’s detection. The time-distance analysis can detect the individual active regions as if they were completely independent.

We have also shown that when an active region is located close to the limb on the near side, a “ghost image” may appear in the far-side image, approximately at its antipode, but relatively weak and smaller in size. Even though this effect is not completely unexpected, it has not been noticed in previous analyses of observational data in both helioseismic holography (Braun & Lindsey 2001) and time-distance helioseismology (Zhao 2007). This is an important finding and gives us hints on when and where features in observational far-side

images may merely be artifacts (i.e. “ghost images”) and are not caused by actual far-side active regions.

We thank Dr. Alan A. Wray and Dr. Konstantin V. Parchevsky for reading this manuscript and their helpful comments.

This work was supported by NASA’s “Living With a Star” program. Support from the NASA Postdoctoral Program administered by Oak Ridge Associated Universities is gratefully acknowledged.

REFERENCES

- Basu, S., Antia, H. M., & Bogart, R. S. 2004, *ApJ*, 610, 1157
- Braun, D. C., & Lindsey, C. 2001, *ApJ*, 560, L189
- Christensen-Dalsgaard, J., et al. 1996, *Science*, 272, 1286
- Christensen-Dalsgaard, J. 2002, *Rev. Modern Phys.*, 72, 1073
- Couvidat, S., Birch, A. C., & Kosovichev, A. G. 2006, *ApJ*, 640, 516
- Duvall, T. L., Jr., Jefferies, S. M., Harvey, J. W., & Pomerantz, M. A. 1993, *Nature*, 362, 430
- Duvall, T. L., Jr., & Kosovichev, A. G. 2001, *Proc. IAU Symp.* 203, 159
- Fan, Y., Braun, D. C., & Chou, D.-Y. 1995, *ApJ*, 451, 877
- González Hernández, I., Hill, F., & Lindsey, C. 2007, *ApJ*, 669, 1382
- Hanasoge, S. M., Larsen, R. M., Duvall, T. L., DeRosa, M. L., Hurlburt, N. E., Schou, J., Christensen-Dalsgaard, J., & Lele, K. 2006, *ApJ*, 648, 1268
- Hartlep, T., & Mansour, N. N. 2005, *Annual Research Briefs–2005*, 357, Center for Turbulence Research, Stanford, California
- Jensen, J. M., Duvall, T. L., Jr., Jacobsen, B. H., & Christensen-Dalsgaard, J. 2001, *ApJ*, 553, L193
- Kosovichev, A. G., Duvall, T. L., Jr., & Scherrer, P. H. 2000, *Sol. Phys.*, 192, 159
- Kosovichev, A. G., & Duvall, T. L., Jr. 1997, *SCORE’96 : Solar Convection and Oscillations and their Relationship*, 225, 241
- Kosovichev, A. G., & Duvall, T. L. 2006, *Space Science Reviews*, 124, 1
- Kravchenko, A. G., Moin, P., & Shariff, K. 1999, *J. Comp. Phys.*, 151, 757
- Lindsey, C., & Braun, D. C. 2000a, *Science*, 287, 1799
- Lindsey, C., & Braun, D. C. 2000b, *Sol. Phys.*, 192, 261
- Lindsey, C., & Braun, D. C. 2005, *ApJ*, 620, 1107

- Loulou, P., Moser, R. D., Mansour, N. N., & Cantwell, B. J. 1997, Technical Memorandum 110436, NASA Ames Research Center, Moffett Field, California
- Norton, A. A., Graham, J. P., Ulrich, R. K., Schou, J., Tomczyk, S., Liu, Y., Lites, B. W., Ariste, A. L., Bush, R. I., Socas-Navarro, H., & Scherrer, P. H. 2006, *Sol. Phys.*, 239, 69
- Parchevsky, K. V., & Kosovichev, A. G. 2007, *ApJ*, 666, 547
- Rhodes, E. J., Kosovichev, A. G., Scherrer, P. H., Schou, J., & Reiter, J 1997, *Sol. Phys.*, 175(2), 287
- Scherrer, P. H., et al. 1995, *Sol. Phys.*, 162, 129
- Sun, M.-T., Chou, D.-Y., & The TON Team 2002, *Sol. Phys.*, 209, 5
- Vernazza, J. E., Avrett, E. H., & Loeser, R. 1981, *ApJS*, 45, 635
- Yee, K. S. 1966, *IEEE Trans. Antenna and Propagation*, 14, 302
- Zhao, J. 2007, *ApJ*, 664, L139
- Zhao, J., & Kosovichev, A. G. 2006, *ApJ*, 643, 1317
- Zharkov, S., Nicholas, C. J., & Thompson, M. J. 2007, *Astronomische Nachrichten*, 328, 240

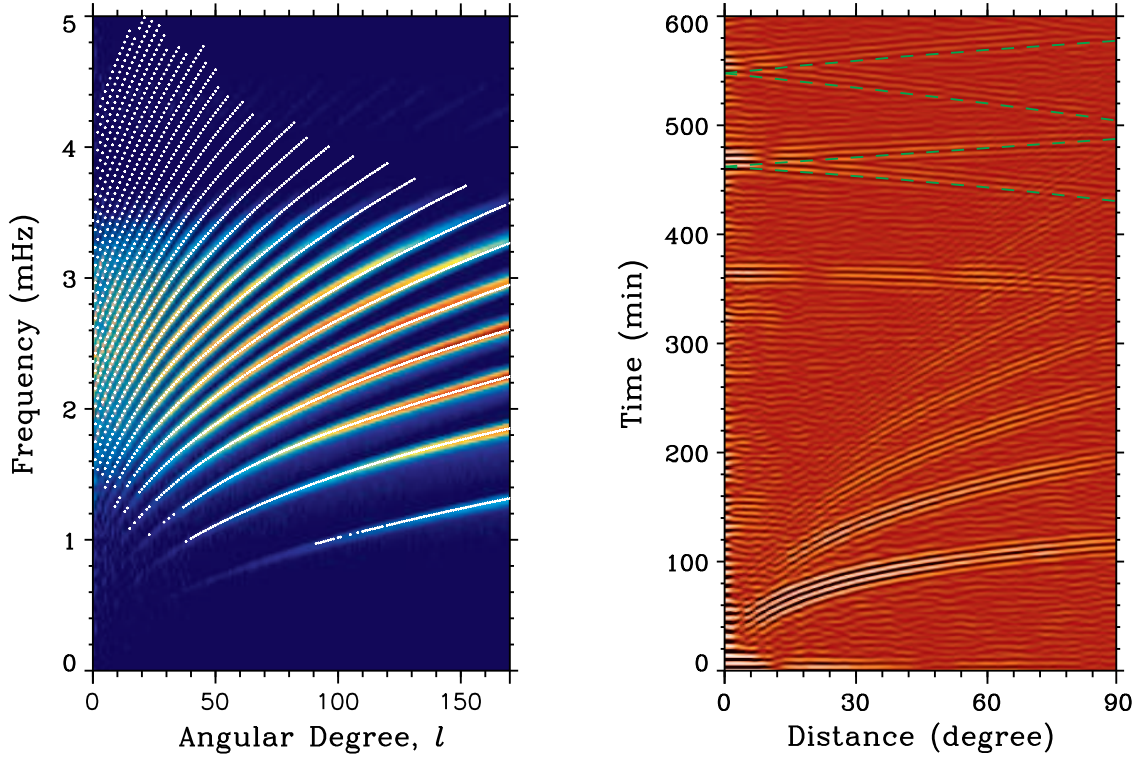


Fig. 1.— The oscillation power spectrum (*left*) and the time-distance diagram (*right*) of a simulated data set. The white dots in the left panel show for comparison the observed frequencies obtained from 144 days of MDI medium- l data using the averaged-spectrum method (Rhodes et al. 1997). The green dashed lines in the right panel indicate the ray-theory predictions for the four-skip and five-skip signals of the acoustic wave packets, which travel from the Earth side to the far side and back to the Earth side

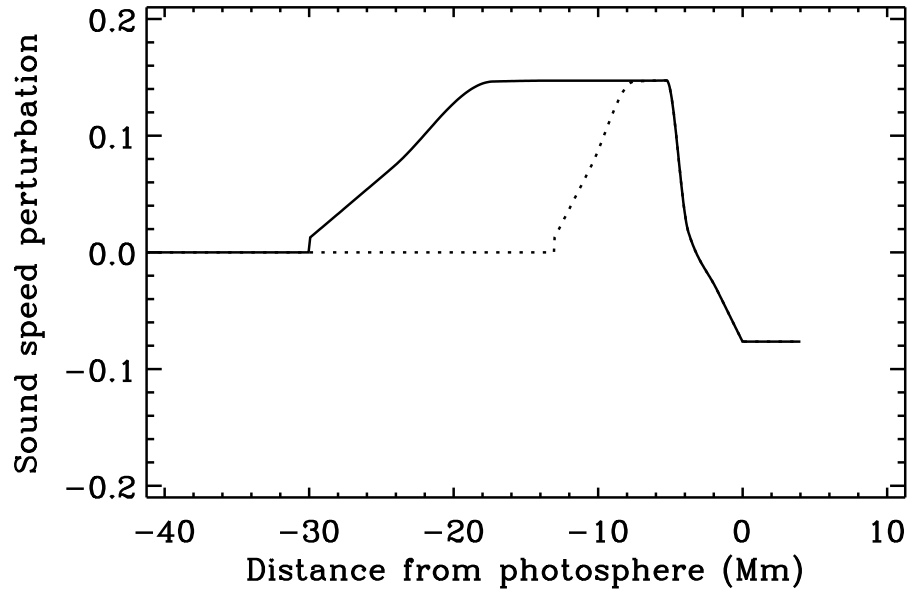


Fig. 2.— The radial profile of the sound speed perturbation in the center of the model active region (*solid curve*), with positive distances denoting locations above the photosphere. The profile was derived by extending the perturbation profile of a sunspot in NOAA active region 8243 on June 18, 1998 (*dotted curve*) inferred from time-distance measurements (Kosovichev et al. 2000). The profile is extended to account for deeper perturbations of large active regions (see text for details).

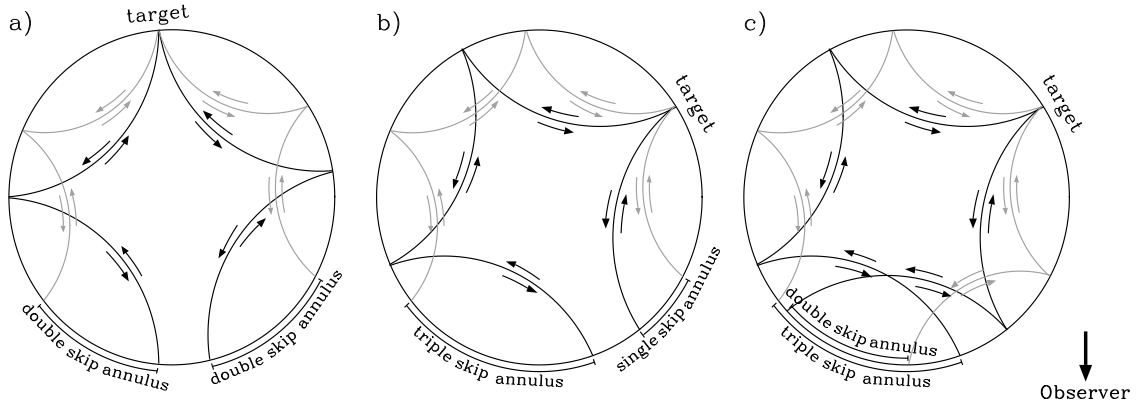


Fig. 3.— Illustrations of the four-skip and five-skip measurement schemes used in the far-side imaging method of Zhao (2007). The skips correspond to the ray paths of acoustic waves traveling between surface points through the solar interior. Specifically, (a) represents the scheme with two skips on either side of the target point, (b) the single-triple skip scheme, and (c) the double-triple skip scheme.

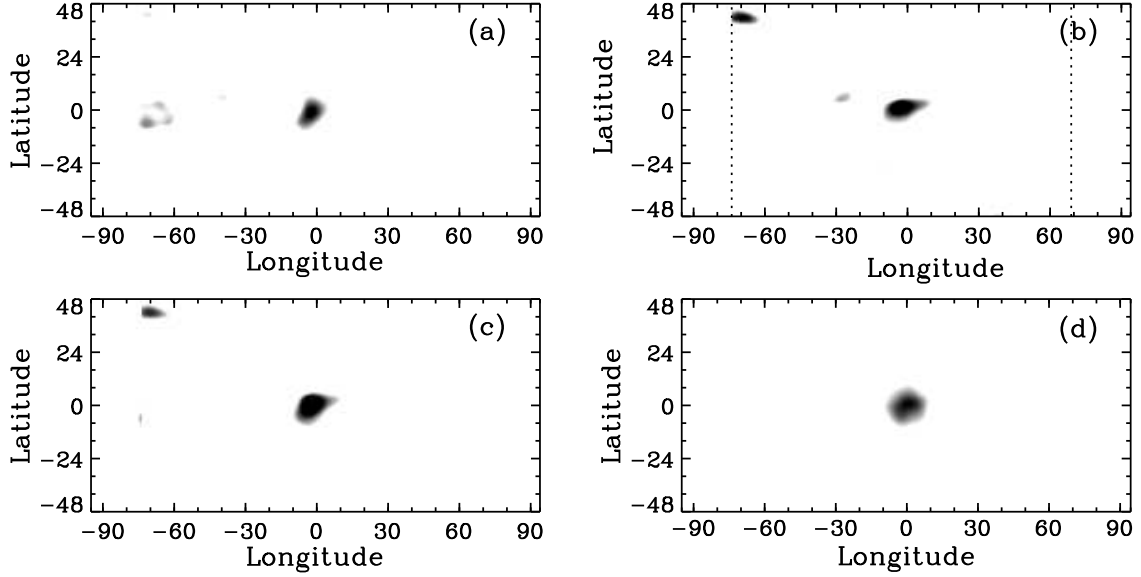


Fig. 4.— Results for an active region with a radius of 90 Mm positioned at the center of the solar far side. The individual panels show: (a) the far-side image from the four-skip measurement scheme, (b) the image from the five-skip scheme, and (c) the combined far-side image. The images show the derived travel-time signals for the different schemes, and are displayed with thresholds of -3.5σ to -2σ , with σ being the standard deviation of the travel time variations (noise level). The dotted lines in panel (b) indicate the spatial limits of the five-skip scheme, which does not cover the whole far side. As an illustration of the actual size and location of the model active region, panel (d) depicts the average acoustic power on the far side computed at the photospheric level. Inside the active region, a reduction in the average acoustic power is observed (*indicated in black*) compared to the quiet Sun (*shown in white*).

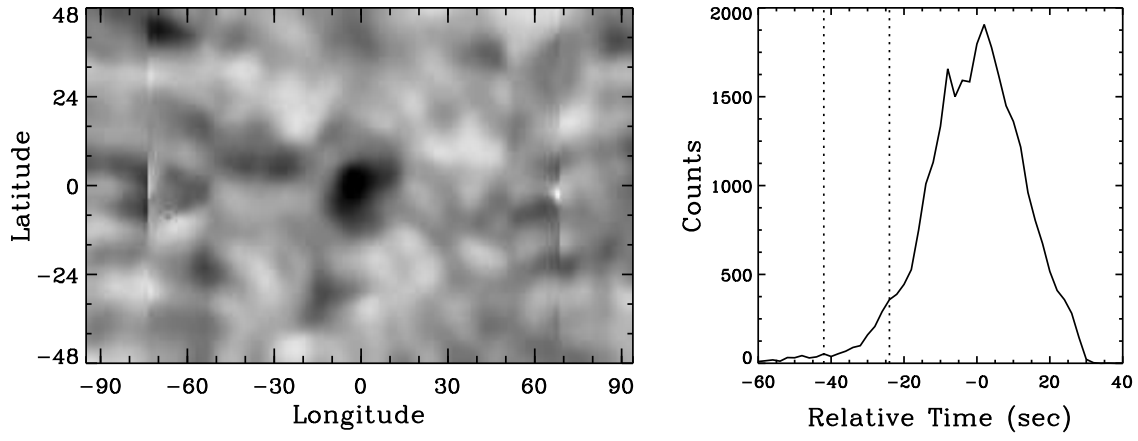


Fig. 5.— The combined method image from Figure 4(c) without thresholding (*left*), and the distribution of travel times residuals in the image (*right*). The dotted lines indicate the threshold limits used for rendering the image in Figure 4(c).

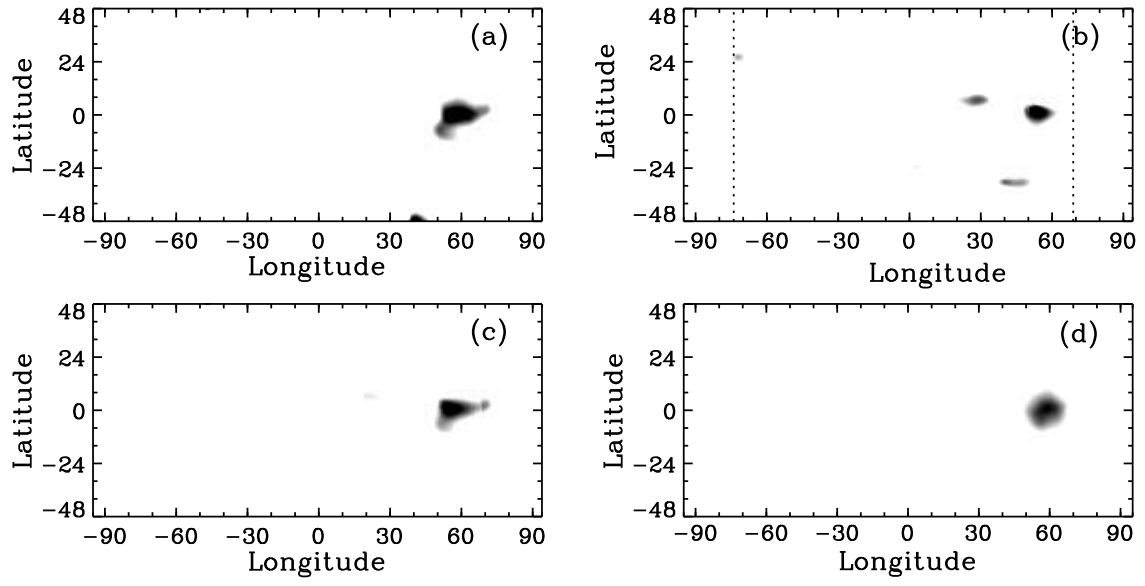


Fig. 6.— Same as Figure 4, except the model active region is placed near the limb of the far side.

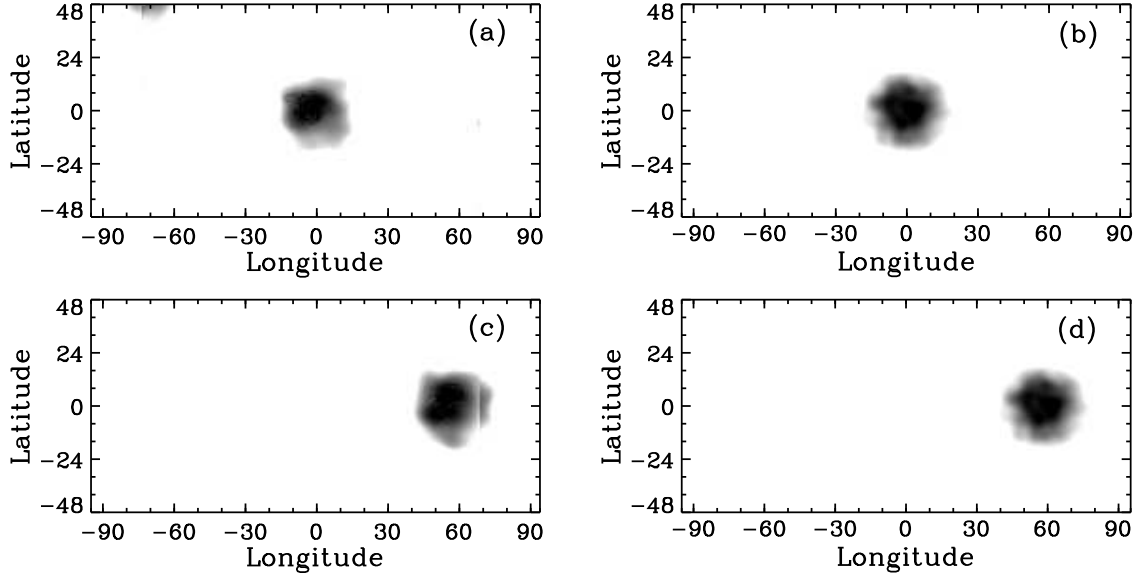


Fig. 7.— Far-side images of a large model active region with a radius of 180 Mm positioned at the center (*a*) and near the limb (*c*) of the far side. The acoustic power at the photosphere for the two cases are shown in panels (*b*) and (*d*), respectively.

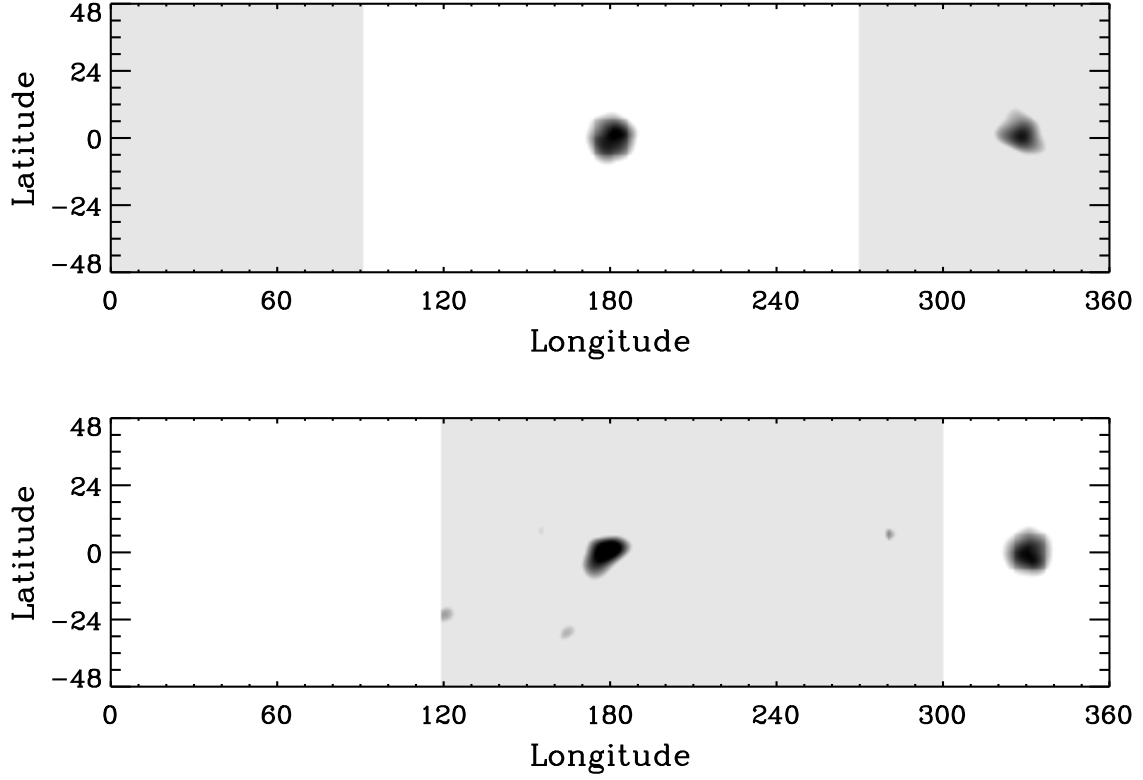


Fig. 8.— Far-side images for a simulation with two medium-sized model active regions at the equator. The two regions are 150° apart longitudinally, namely, at 180° and 330° . For the two panels, two different regions have been selected as the near side. The panels depict a combination of the acoustic power map of the near-side (*white background*), and the far-side map (*gray background*) computed from the oscillation data on the near side.

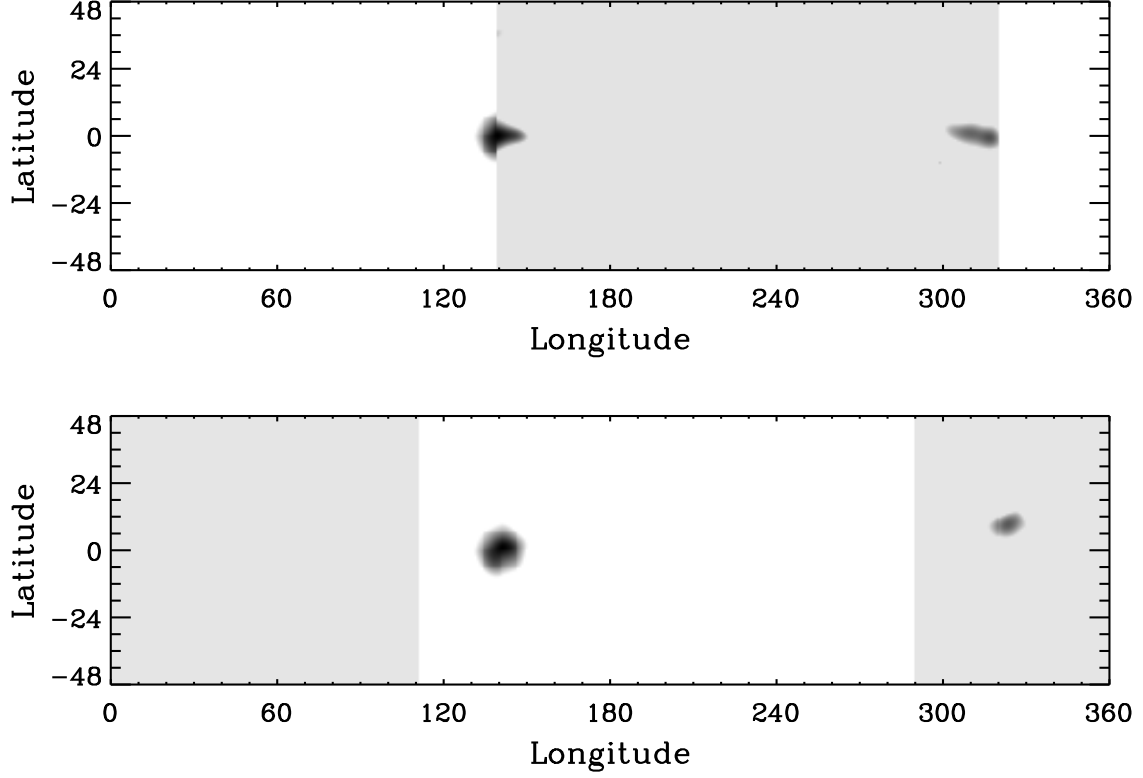


Fig. 9.— Far-side images for a simulation with a single, 90 Mm-radius model active region. The active region is placed at a longitude of 140° . Its smaller and weaker “ghost image” can be found at approximately 320° in both panels. Similarly to Figure 8, two different parts of the surface have been selected as the near side for the two panels, and again show a combination of the acoustic power maps of the near side (*white background*) and the far-side image (*gray background*).